Mathematics and Systems Science 2025, 3(2), 3093.
https://doi.org/10.54517/mss3093

Article

The numerical investigation of the time-dependent Couette flow of dusty Casson fluid generated by parallel Riga plates

S. Nasrin[1], M. R. Islam[2,*], R. N. Mondal[1], M. M. Alam[3]

[1] Department of Mathematics, Jagannath University, Dhaka 1100, Bangladesh
[2] Department of Mathematics, Bangabandhu Sheikh Mujibur Rahman Science and Technology University, Gopalganj 8100, Bangladesh
[3] Khulna University, Khulna 9208, Bangladesh
*** Corresponding author:** M. R. Islam, mribsmrstu@yahoo.com

CITATION

Nasrin S, Islam MR, Mondal RN, Alam MM. The numerical investigation of the time-dependent Couette flow of dusty Casson fluid generated by parallel Riga plates. Mathematics and Systems Science.2025; 3(2): 3093. https://doi.org/10.54517/mss3093

ARTICLE INFO

Received: 23 November 2024
Accepted: 6 March 2025
Available online: 9 April 2025

Abstract: This research explores the impact of the relative magnetic effect on the Couette flow of dusty Casson fluid between two parallel Riga plates. The mathematical model is based on a set of partial differential equations that describe the behavior of the dusty Casson fluid in interaction with the Riga plate. To convert this system of equations to its dimensionless form, appropriate transformations are used, and to solve this system numerically, explicit finite difference methods are applied to it. A graphical representation has been presented by using MatLab software for a comprehensive understanding of the effect of various non-dimensional parameters such as pressure gradient parameter (α), Casson parameter (β), modified Hartmann number (H_a), fluid concentration parameter (R), particle mass parameter (G), Eckert number (E_c), Prandtl number (P_r), and temperature relaxation time parameter (L_0) on the velocity distributions u (or u_p) and on the temperature distributions θ (or θ_p), including shear stress and Nusselt number for both clean and dust fluid particles. The impacts of these parameters on the above-mentioned distributions have been discussed with their physical significance, taking the variation of any one of those parameters and with fixed values of α =1, β = 2, H_a=1, R = 0.5, G = 0.5, E_c = 0.01, P_r = 0.71, and L_0 =0.8. The results reveal significant effects of relative magnetic fields on both clean fluid and dust particle motion.

Keywords: Couette flow; Riga plate; Casson fluid; magnetic field; dust particle; explicit finite difference

1. Introduction

A Casson fluid is a type of non-Newtonian fluid characterized by its unique flow behavior. In 1959, Casson [1] introduced this concept to describe the behavior of fluids exhibiting yield stress. A Casson fluid remains in a solid-like state until a certain level of stress, known as the yield stress, is applied. A Riga plate, which generates an electromagnetic field through embedded electrodes and magnets, can modify the behavior of non-Newtonian fluids, including Casson fluids. In such fluids, Riga plates help optimize flow control, heat transfer, air pollution management, and biomedical applications. Finally, the electromagnetic properties of the Riga plate make it an important tool for enhancing performance and control in processes involving Casson fluids across a variety of industrial and biomedical fields. Gailitis and Leilausis [2] first introduced the Riga plate, which creates a Lorentz force parallel to the wall to control fluid flow. The inclusion of the Greenberg term has garnered significant interest, leading to several studies on the Riga plate. Saffman [3] developed equations for the fluid flow of dust particles, illuminating the interactions between particles under laminar flow conditions and improving the understanding of how suspended

particles affect fluid behavior. A major challenge in fluid mechanics is understanding the dynamics of fluids containing dispersed particles. Eldabe et al. [4] investigated heat transfer in a stationary, incompressible, electrically conducting non-Newtonian Casson fluid between two rotating cylinders exposed to a radial magnetic field. Fang [5] studied the effect of uniform suction or injection on unsteady incompressible Couette flow using the Eyring-Powell equation. Non-Newtonian fluids, such as Casson fluids, exhibit unique properties, which have generated considerable interest due to their wide application in engineering. Boyd et al. [6] used the Casson and Carreau-Yasuda models in their non-Newtonian blood viscosity experiments. Damseh [7] explored the flow of a viscous, incompressible gas containing dust around an isothermal cylinder, simplifying the analysis by assuming a uniform distribution of particles to better understand their effects on flow dynamics. In a separate study, Makinde and Chinyoka [8] investigated the transient flow of a magnetohydrodynamic (MHD) fluid characterized by temperature-dependent viscosity and thermal conductivity. Eguia et al. [9] examined the flow and heat transfer properties of a dusty fluid between parallel plates under a magnetic field with high accuracy. Hyatt et al. [10] analyzed the Soret and Dufour effects in the MHD flow of a Casson fluid over a stretching surface. Nadeem et al. [11] focused on the two-dimensional flow of an MHD Casson fluid over a porous, linearly stretching sheet. The Riga plate produces electromagnetic hydrodynamic behavior, reducing both friction and pressure drag. This technology finds numerous applications, including cell separation, magneto-dynamics, electro-hydrodynamic flow control, marine and geological technology, biomechanics, and magnetic devices for various industrial processes. Ramesh and Gireesha [12] studied the effects of radiation on the steady, two-dimensional boundary layer flow of a dusty fluid over an expanding sheet, while Mukhopadhyay et al. [13] investigated the dynamic behavior of a non-Newtonian fluid undergoing two-dimensional flow over an extended surface with a fixed surface temperature. Attia et al. [14] analyzed unsteady MHD flow and heat transfer in a dusty particle confined between two infinite horizontal plates, specifically examining how temperature-dependent properties affect fluid dynamics and heat transfer. The application of a magnetic field changes the motion of charged particles in the fluid. In the dusty Casson fluid, the magnetic field exerts a Lorentz force on the charged dust particles, affecting their distribution and motion. Pramanik [15] examined the boundary layer dynamics and heat transfer of a non-Newtonian fluid moving towards an exponentially expanding surface using the Casson model, incorporating surface suction or blowing effects. Ramesh and Devakar [16] analyzed three main flow modes—Couette, Poiseuille, and Generalized Couette—in an incompressible case fluid between parallel plates. Abbas et al. [17] investigated entropy generation in nanofluid flow over a horizontal Riga plate. Raju et al. [18] studied the heat and mass transfer properties of a Casson fluid over a rapidly permeable stretching surface, providing valuable insights into transport phenomena in fluid dynamics. Awais et al. [19] used numerical methods to explore mass and heat transfer in two-dimensional, steady, laminar, and incompressible fluid flow within a non-Newtonian fluid model near a stretching surface. Isa and Mohammed [20] analyzed the boundary layer flow of a dusty viscous fluid over a stationary sheet of another dusty viscous fluid, emphasizing the interaction between the two. Jalil et al. [21] examined the boundary layer behavior of an

electrically conducting dusty fluid over a stretching surface, considering the effect of an applied magnetic field to understand how these factors interact in fluid flow. Anjum et al. [22] explored the dynamics of a thermally stratified viscous fluid experiencing stagnation point flow over a nonlinear Riga plate of varying thickness. Ismail et al. [23] studied the effects of dust particles on the velocity of an electrically conducting viscous fluid flowing between parallel permeable plates under a transverse magnetic field, elucidating how suspended particles affect fluid dynamics in this configuration. Ahmad [24] investigated mixed convection in nanofluids near a vertical Riga plate, accounting for significant suction effects. Attia and Ewis [25] analyzed the effects of continuous dusty viscous particles and a convective power-law fluid on both fluid and particle phase velocities, as well as skin friction, under the influence of Darcy resistive forces. Recently, Khan et al. [26] examined the slip effect on the behavior of a Casson dust fluid in a two-phase fluctuating flow over an inclined parallel plate, highlighting the relative magnetic field effect and the complex interactions within the system. Jalili et al. [27] investigated a fluid characterized by non-Newtonian Casson behavior, incompressibility, temperature-dependent viscosity, and magneto-hydrodynamic (MHD) properties. Their study focused on fluid flow within a rectangular channel formed by two parallel, permeable plates capable of expansion and contraction. Khan et al. [28] explored the Graetz problem for a Casson fluid model subjected to a prescribed heat flux in a circular duct. Khan and Ali [29] analyzed the classical Graetz problem for a fluid governed by the Casson constitutive equation, which is particularly relevant for describing the thermal entry flow of blood within a duct. Khan et al. [30] examined the influence of axial conduction and viscous dissipation on heat transfer inside a tube, utilizing the Casson fluid model. A semi-analytical approach was employed to tackle the problem. Ashish et al. [31] examined the stagnation point flow and heat transfer characteristics of MHD boundary layer Casson hybrid nanofluid as it passes through a porous medium around an exponentially stretched cylinder.

As a non-Newtonian fluid, the viscosity of Casson fluid varies with the applied shear rate. Its flow behavior primarily depends on this viscosity and is generally unaffected by electric or magnetic fields. However, under certain conditions, when subjected to an electric or magnetic field that facilitates the movement of charged particles, the influence of relevant parameters on the Casson fluid becomes noticeable. Few studies have explored the flow of Casson fluid through the Riga plate. In this context, the objective of this study is to analyze the Couette flow behavior generated by parallel Riga plates in a dusty Casson fluid under the influence of the electromagnetic field produced by the Riga plates.

2. Mathematical formulation

Consider the unsteady flow of an incompressible dusty Casson fluid between two horizontal parallel Riga plates, where one plate is in motion while the other remains stationary. The lower plate is fixed at $\hat{y} = 0$, while the upper plate moves at a constant velocity U_0 and is separated from the lower plate by a distance $\hat{y} = h$. The flow direction is aligned with the $\hat{x}$-axis, while the $\hat{y}$-axis is perpendicular to the flow, and the plate's width runs parallel to the $\hat{z}\hat{x}$-plane. Due to the use of a Riga plate, a Lorentz force is generated by the interaction of electric and magnetic forces. According to the

Grinberg hypothesis, the Lorentz force is described concerning the magnetic field associated with the Riga plate as follows:

$$\hat{f} = \boldsymbol{J} \wedge \boldsymbol{B} = \left(\frac{\pi}{8} J_0 M_0 e^{-\frac{\pi}{l}\hat{y}} \quad , \quad 0 \quad , \quad \frac{\pi}{8} J_0 M_0 e^{-\frac{\pi}{l}\hat{y}}\right) \tag{1}$$

where, $\boldsymbol{J}$ is the current density vector, $\boldsymbol{B}$ is the induced magnetic field vector, and l is the width of the electrode or magnet.

And for an isotropic and incompressible flow of a Casson fluid, the rheological equation is defined by:

$$\left.\begin{aligned} \tau_{ij} &= \left(\mu_b + \frac{p_y}{\sqrt{2\pi}}\right) 2e_{ij} \text{ when } \pi > \pi_c, \\ \tau_{ij} &= (\mu_b + \frac{p_y}{\sqrt{2\pi_c}}) 2e_{ij} \text{ when } \pi < \pi_c \end{aligned}\right\} \tag{2}$$

where,$\tau_{ij}$the shear stress; $p_y = \frac{\mu_b\sqrt{2\pi}}{\beta}$; $\mu_b$is the plastic viscosity of the non-Newtonian fluid; e_{ij} is the (i, j) -th component of the deformation rate is defined, with $\pi_c$representing the critical value derived from the non-Newtonian model. In the context of a Casson fluid, which is a type of non-Newtonian fluid, where $\pi > \pi_c$, the dynamic viscosity is represented by $\mu = \mu_b + \frac{p_y}{\sqrt{2\pi}}$while the kinematic viscosity is denoted as $\upsilon = \upsilon_b \left(1 + \frac{1}{\beta}\right)$ where,$\upsilon_b = \frac{\mu_b}{\rho}$ and β is the Casson parameter. The fluid is driven by the combined action of pressure gradient $\frac{\partial \hat{p}}{\partial \hat{x}}$and Lorentz force. According to the parallel Couette flow, the velocity components$\hat{u} \neq 0, \hat{u}_p \neq 0, \hat{v} = \hat{v}_p = \hat{w} = \hat{w}_p = 0$ and $\frac{\partial}{\partial \hat{z}} = 0$for the clean and dust particles.For the clean fluid phase, the continuity equation reduces to $\frac{\partial \hat{u}}{\partial \hat{x}} = 0$ which gives $\hat{u} = \hat{u}(\hat{y}, \hat{t})$ and for the dust phase $\frac{\partial \hat{u}_p}{\partial \hat{x}} = 0$ gives $\hat{u}_p = \hat{u}_p(\hat{y}, \hat{t})$. The temperature $T_1$for the lower plate and $T_2$for the upper plate, where $T_2 > T_1$. The physical model is illustrated in **Figure 1**.

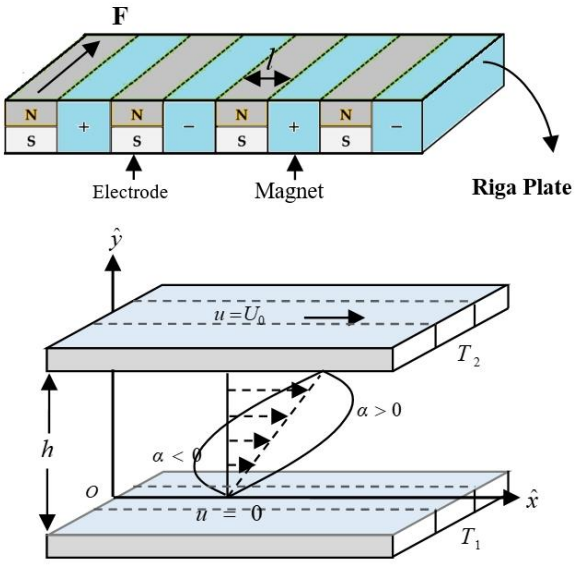

Figure 1. Physical model and coordinate system.

Given the aforementioned assumptions, the set of coupled non-linear partial differential equations for the fluid phase and the dust particles describes the equations as follows:

$$\frac{\partial \hat{u}}{\partial \hat{t}} = -\frac{P}{\rho} + \upsilon_b \left(1 + \frac{1}{\beta}\right)\frac{\partial^2 \hat{u}}{\partial \hat{y}^2} + \frac{\pi}{8\rho} J_0 M_0 e^{-\frac{\pi}{l}\hat{y}} - \frac{1}{\rho} KN(\hat{u} - \hat{u}_p) \tag{3}$$

$$\frac{\partial T}{\partial \hat{t}} = \frac{k}{\rho c_p}\frac{\partial^2 T}{\partial \hat{y}^2} - \frac{1}{\rho c_p}\frac{2kKN}{3\mu_b}(T - T_p) + \frac{\mu_b}{\rho c_p}\left(1 + \frac{1}{\beta}\right)\left(\frac{\partial \hat{u}}{\partial \hat{y}}\right)^2 \tag{4}$$

$$m_p \frac{\partial \hat{u}_p}{\partial \hat{t}} = KN(\hat{u} - \hat{u}_p) \tag{5}$$

$$\frac{\partial T_p}{\partial \hat{t}} = \frac{4k\pi aN}{\rho_p c_s}(T - T_p) \tag{6}$$

The corresponding boundary conditions are:

$$\begin{aligned} &\hat{t} = 0: \hat{u} = \hat{u}_p = 0, T = T_1, \text{for all } \hat{y} \\ &\hat{t} > 0: \begin{cases} \hat{u} = 0,\ \hat{u}_p = 0, T = T_1, T_p = T_1 \text{at } \hat{y} = 0 \\ \hat{u} = U_0,\ \hat{u}_p = U_0, T \to T_2,\ T_p \to T_2 \text{at } \hat{y} \to h \end{cases} \end{aligned} \tag{7}$$

where, J_0 is the constant current density, M_0 is the induced magnetic field strength, $\hat{u}$ and $\hat{u}_p$ are the clean fluid and dust particles velocity components, υ is the kinematic viscosity of the clean fluid, ρ_p is the material density (or mass per unit volume) of dust particles,N is the number of dust particles per unit volume, κ is the permeability of the porous medium, and k is the thermal conductivity of the fluid, K is the Stokes constant $= 6\pi\rho\upsilon a$;a is the average radius of the dust particles, m_p is the average mass of the dust particles, c_s is the is the specific heat capacity of the fluid particles, c_p is the specific heat capacity at constant pressure, T is the temperature of the fluid, T_p is the temperature of the dust particles, γ_T is the temperature relaxation time, which is defined by $\gamma_T = \frac{\rho_p c_s}{4k\pi aN}$ or $\frac{3\rho\upsilon\rho_p c_s}{2kKN}$.

2.1. Non-dimensional analysis

To simplify the analysis, the following non-dimensional variables are introduced, which enable the above equations to be converted to their dimensionless form.

$$\hat{x} = \frac{x}{h}, \quad \hat{y} = \frac{y}{L}, \quad \hat{u} = \frac{u}{U_0}, \quad \hat{t} = \frac{tU_0}{h}, \quad \theta = \frac{T - T_2}{T_1 - T_2},$$

$$\theta_p = \frac{T_p - T_2}{T_1 - T_2}, \quad h = \frac{L^2 U_0}{\upsilon_b}, \quad L = \frac{l}{\pi} \text{and} U_0 = \frac{\upsilon_b}{l}.$$

By applying these non-dimensional variables to the above equations from Equation (3) to Equation (6) together with the boundary conditions (7) and removing the cap notation from the variables, the governing equations are transformed into the following non-dimensional form:

$$\frac{\partial u}{\partial t} = \alpha + \left(1 + \frac{1}{\beta}\right)\frac{\partial^2 u}{\partial y^2} + H_a e^{-y} - R\left(u - u_p\right) \tag{8}$$

$$\frac{\partial \theta}{\partial t} = \frac{1}{P_r}\frac{\partial^2 \theta}{\partial y^2} - \frac{2R}{3P_r}\left(\theta - \theta_p\right) + E_c\left(1 + \frac{1}{\beta}\right)\left(\frac{\partial u}{\partial y}\right)^2 \tag{9}$$

$$\frac{\partial u_p}{\partial t} = \frac{1}{G}\left(u - u_p\right) \tag{10}$$

$$\frac{\partial \theta_p}{\partial t} = L_0\left(\theta - \theta_p\right) \tag{11}$$

With the corresponding boundary conditions,

$$\left.\begin{array}{l} t = 0: u = u_p = 0, \theta = 0, \text{for all} y \\ t > 0: \begin{cases} u = 0, u_p = 0, \theta = 1, \theta_p = 1 \text{at} y = 0 \\ u = 1, u_p = 1, \theta \to 0, \theta_p \to 0 \text{at} y \to h \end{cases} \end{array}\right\} \tag{12}$$

where,

$\alpha = -\frac{hP}{\rho U_0^2}$is the dimensionless pressure gradient;

$H_a = \frac{\pi J_0 M_0 h}{8\rho U_0^2}$is the modified Hartmann number;

$E_c = \frac{h\mu_b U_0}{c_p L^2 (T_w - T_\infty)} = \frac{U_0^2}{c_p (T_w - T_\infty)}$ is the Eckertnumber;

$P_r = \frac{\rho c_p \upsilon_b}{k}$is the Prandtl number;

$\beta = \frac{\mu_b \sqrt{2\pi}}{p_y}$ = Casson parameter;

$G = \frac{m_p U_0}{hKN}$is the particle mass parameter;

$R = \frac{hKN}{\rho U_0} = \frac{KN}{\rho}\frac{l^2}{\pi^2 \upsilon_b} = \frac{KNl^2}{\mu_b \pi^2}$is the particle concentration parameter;

$L_0 = \frac{h}{\gamma_T U_0}$is the temperature relaxation time parameter.

2.2. Shear stresses and Nusselt number

The impact of key parameters on the local and average shear stress based on the velocities of both the fluid phase and the dust particles has been explored. Since the shear stress is proportional to the velocity gradient, therefore in the fluid phase the non-dimensional formulations for the local shear stress are expressed as:

$$\tau_L = \mu \left.\frac{\partial u}{\partial y}\right|_{y=0} \text{ and } \tau_L = \mu \left.\frac{\partial u}{\partial y}\right|_{y=h} \tag{13}$$

and average shear stress are:

$$\tau_A = \frac{1}{L}\int_0^L \mu \left.\frac{\partial u}{\partial y}\right|_{y=0} dx \text{and} \tau_A = \frac{1}{L}\int_0^L \mu \left.\frac{\partial u}{\partial y}\right|_{y=h} dx \tag{14}$$

And for the dust particle local, shear stress is defined as:

$$\tau_{pL} = \mu \frac{\partial u_p}{\partial y}\Big|_{y=0} \text{ and } \tau_{pL} = \mu \frac{\partial u_p}{\partial y}\Big|_{y=h} \tag{15}$$

and average shear stress are:

$$\tau_{pA} = \frac{1}{L}\int_0^L \mu \frac{\partial u_p}{\partial y}\Big|_{y=0} dx \text{ and } \tau_{pA} = \frac{1}{L}\int_0^L \mu \frac{\partial u_p}{\partial y}\Big|_{y=h} dx \tag{16}$$

Again, another key parameter for the temperature, the Nusselt number, is defined by the rate of heat transfer flow from the plates to the fluid. In fluid phase, the non-dimensional formulations of the local Nusselt numbers are expressed as:

$$Nu_L = -\mu \frac{\partial \theta}{\partial y}\Big|_{y=0} \text{ and } Nu_L = -\mu \frac{\partial \theta}{\partial y}\Big|_{y=h} \tag{17}$$

and average Nusselt numbers are

$$Nu_A = -\frac{1}{L}\int_0^L \mu \frac{\partial \theta}{\partial y}\Big|_{y=0} dx \text{ and } Nu_A = -\frac{1}{L}\int_0^L \mu \frac{\partial \theta}{\partial y}\Big|_{y=h} dx \tag{18}$$

And for the dust particle, local Nusselt numbers are defined as

$$Nu_{pL} = -\mu \frac{\partial \theta_p}{\partial y}\Big|_{y=0} \text{ and } Nu_{pL} = -\mu \frac{\partial \theta_p}{\partial y}\Big|_{y=h} \tag{19}$$

and average Nusselt numbers are

$$Nu_{pA} = -\frac{1}{L}\int_0^L \mu \frac{\partial \theta_p}{\partial y}\Big|_{y=0} dx \text{ and } Nu_{pA} = -\frac{1}{L}\int_0^L \mu \frac{\partial \theta_p}{\partial y}\Big|_{y=h} dx \tag{20}$$

The investigation of the local and average shear stress and Nusselt numbers is displayed only for the lower plate in the result and discussion Section-4.

3. Method of solution

The system of non-dimensional coupled partial differential Equations (8)–(11) is solved using a definite finite difference method subject to the specified boundary conditions in Equation (12). In this case, the range extends from 0 to 10, while the range is from 0 to 2. Finite difference schemes related to this problem are presented as follows:

$$u_{i,j}^{k+1} = u_{i,j}^k + \alpha\Delta t + \frac{\Delta t}{\Delta y^2}\left(1+\frac{1}{\beta}\right)\left(u_{i,j+1}^k - 2u_{i,j}^k + u_{i,j-1}^k\right) + H_a\Delta t e^{-y}{}_i - R\Delta t\left(u_{i,j}^k - {u_p}_{i,j}^k\right) \tag{21}$$

$$\theta_{i,j}^{k+1} = \theta_{i,j}^k + \frac{\Delta t}{P_r\Delta y^2}\left(\theta_{i,j+1}^k - 2\theta_{i,j}^k + \theta_{i,j-1}^k\right) - \frac{2R\Delta t}{3p_r}\left(\theta_{i,j}^k - {\theta_p}_{i,j}^k\right) - \frac{E_c\Delta t}{\Delta y}\left(1+\frac{1}{\beta}\right)\left(u_{i,j}^k - u_{i,j-1}^k\right) \tag{22}$$

$${u_p}_{i,j}^{k+1} = {u_p}_{i,j}^k + \frac{\Delta t}{G}\left(u_{i,j}^k - {u_p}_{i,j}^k\right) \tag{23}$$

$${\theta_p}_{i,j}^{k+1} = {\theta_p}_{i,j}^k + \Delta t L_0\left(\theta_{i,j}^k - {\theta_p}_{i,j}^k\right) \tag{24}$$

With the boundary conditions.

$$\left.\begin{aligned} U_{i,L} = 0, U_{p_{i,L}} = 0, \theta_{i,L} = 1, \theta_{p_{i,L}} = 1 \text{at} L = 0 \\ U_{i,L} = 1, U_{p_{i,L}} = 1, \theta_{i,L} = 0, \theta_{p_{i,L}} = 0 \text{at} L = 1 \end{aligned}\right\} \quad (25)$$

Here, the subscripts i and j refer to x and y, and the superscript k refers to time τ.

4. Results and discussion

To analyze the physical situation of the problem, graphical representations have been illustrated with the effects of the non-dimensional parameters such as pressure gradient parameter (α), the dimensionless Casson parameter (β), modified Hartmann number (H_a), fluid concentration parameter (R), particle mass parameter(G), Eckert number (E_c), Prandtl number (P_r), and temperature relaxation time parameter (L_0) on the velocity distributions u(or u_p) and on the temperature distributions θ(or θ_p). The impacts of these parameters on the above-mentioned distributions have been discussed with its physical significance taking the variation of any one of those parameters and with fixed values of α=1, β =2, H_a=1, R =0.5, G =0.5, E_c =0.01,P_r =0.71, and L_0 =0.8.

4.1. Time and mesh sensitivity test

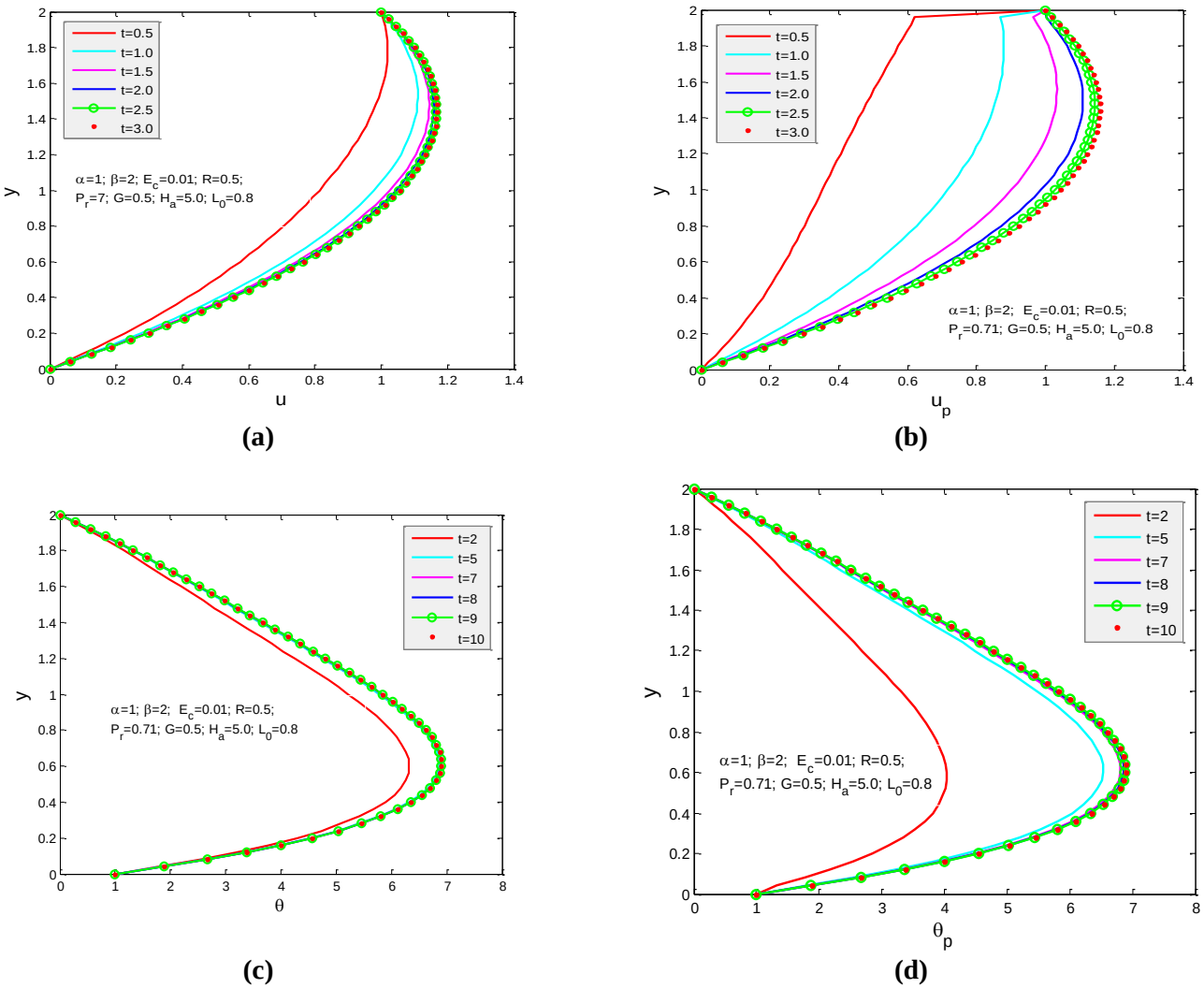

Figure 2. Time sensitivity on the **(a)** velocity u; **(b)** velocity u_p; **(c)** temperature θ; **(d)** temperature θ_p.

Before executing the program, it has been introduced with time and mesh sensitivity analysis. To obtain the steady-state solution, it is necessary to examine the velocity and temperature distributions at different times. **Figure 2a**,**b** show the fluid velocity distribution u for clean fluid and u_p for dusty fluid at different times. Calculations were made for the velocity profiles at times t = 0.5,1.0,1.5,2.0,2.5, and 3 using a time step size of Δt=0.0005. The figures indicate minimal changes in the velocity distributions of u and u_p after time t=3. Similarly, **Figure 2c**,**d** show the time sensitivity for the temperature distribution θ and θ_p for the dust temperature at the times$t$=2,5,7,8,9, and 10. Here the minimal changes have occurred after t=10.

Figure 3a,**b** presented the validation of the grid pairs on the velocity distributions $u$and u_p. It has shown the velocity distribution for three grid pairs$(m,n) = (40,40)$, $(m,n) = (50,50)$and $(m,n) = (60,60)$ with time$t = 3$ and time step$\Delta t = 0.0005$. and **Figure 3c**,**d** illustrate the validity of the grid pairs on the temperature distributions θ and θ_p. There is a minimal variation among these grid pairs, making any single grid pair suitable for obtaining the steady-state solution. This observation holds true for the other distributions. The steady-state solution has performed at least $t > 7$ for temperature distributions. In the present study, the following graphs have been established for the choice of time $t = 3$ for velocity distributions and $\tau = 10$ temperature distributions with the grid pair $(m,n) = (50,50)$ and time step $\Delta t = 0.0005$.

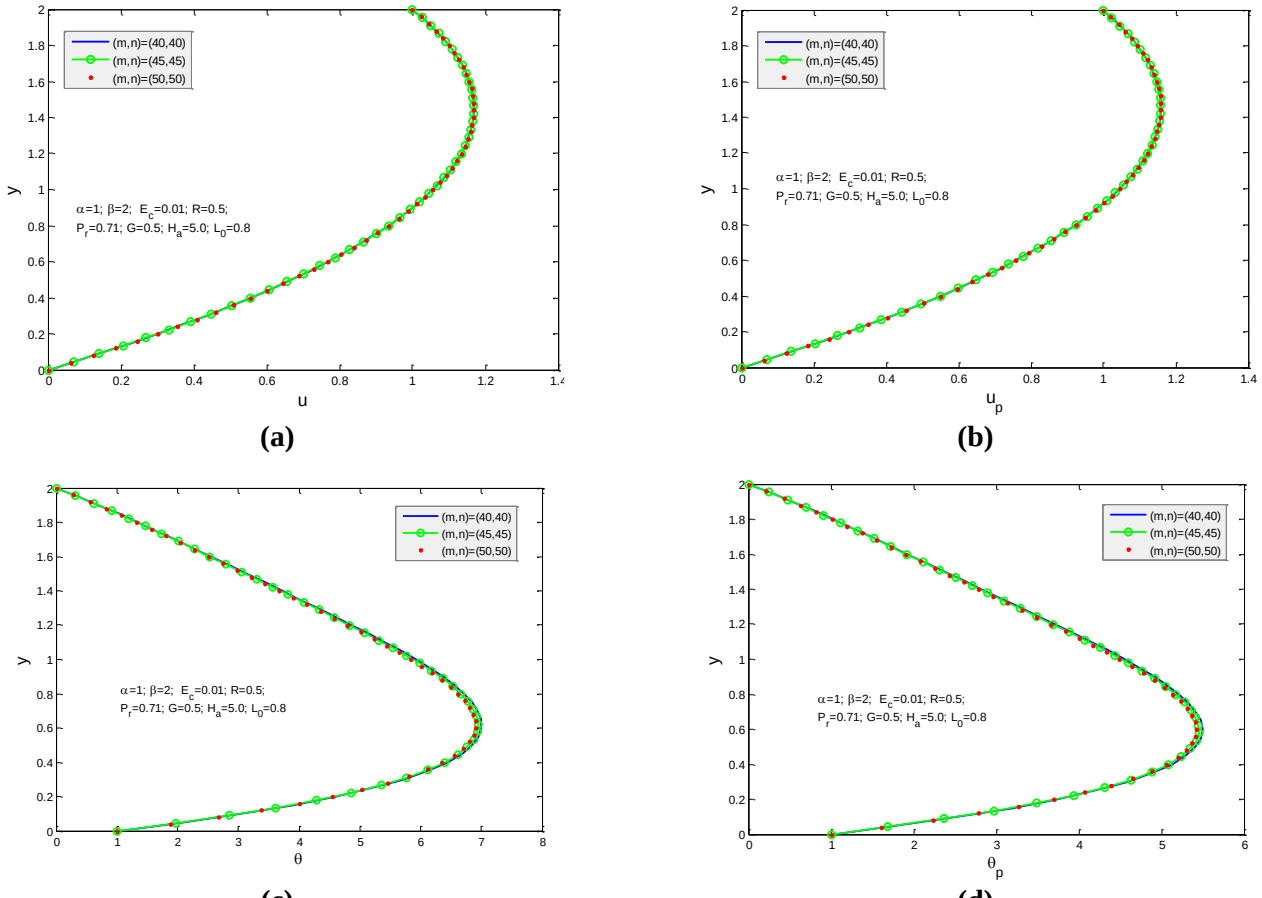

Figure 3. Mesh sensitivity on the **(a)** velocity u; **(b)** velocity u_p; **(c)** temperature θ; **(d)** temperature θ_p.

4.2. Validation test

Before discussing the impact of the pertinent parameters on the velocity and temperature distributions, it is required to verify the present results. To do this, the present numerical results have been compared with the previously published result graphically as follows:

Figure 4a illustrates the effect of pressure gradient parameters such as α = −3, −2, −1, 0, 1, 2, and 3 on the velocity of the clean fluid in the absence of a magnetic field. In contrast, **Figure 4b** illustrates velocity distributions for the same values of the pressure gradient parameter in the absence of the Casson parameter and the modified Hartmann number, that is, the absence of a magnetic parameter with the fixed values of G=0.5, P_r =0.71, E_c=0.01, and L_0 = 0.8. The same behavior has likely been observed in both figures. Therefore, it has been decided that our numerical result is qualitatively acceptable to the present investigation.

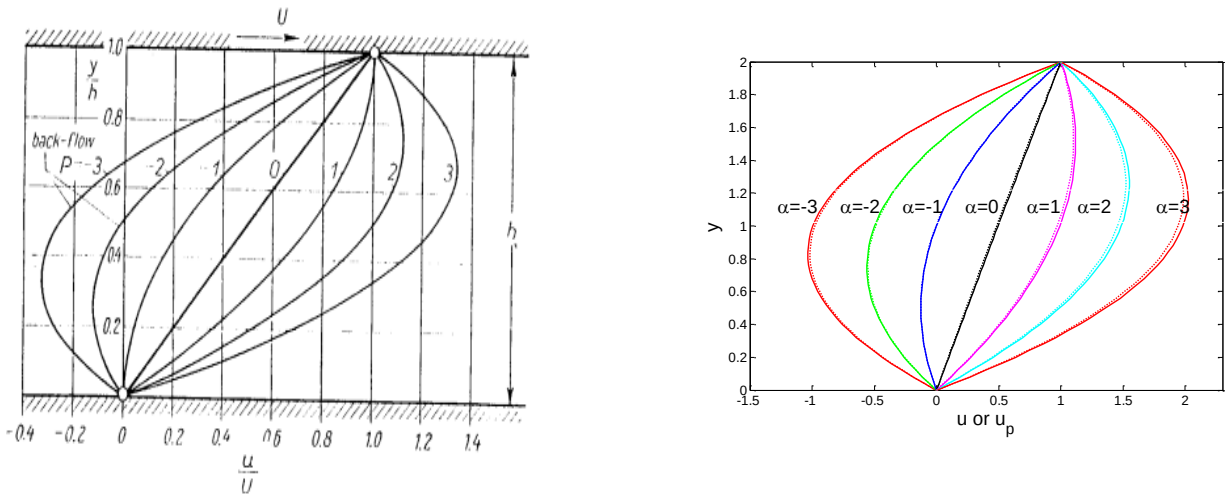

(a) **(b)**

Figure 4. Effect of αonvelocity **(a)** published results [well-known book-boundary layer theory by H. Schlichting]; **(b)** present numerical results in the absence of β, H_a, and with fixed G = 0.5, P_r = 0.71, E_c = 0.01, and L_0 = 0.8.

4.3. Impacts of various parameters

To examine the physical context of the problem, it is important to note that in each figure from **Figures 5–17**, the solid line illustrates the distribution of the clean fluid phase, whereas the dotted line represents the distribution of the dust particle phase.

4.3.1. Impacts of relevant parameters on velocity, local shear stress and average shear stress

Figures 5–10 illustrate the distribution of velocity, the local and average shear stressfor various values of α, β, H_a, G,and R.

The effect of the dimensionless pressure gradient parameter (α) on the velocities of both the clean phase and dust particles is illustrated in **Figure 5a–c**. When α> 0, there is a pressure decrease in the direction of motion, leading to an increase in velocity across the entire space between the plates as the gradient intensifies. It increases the transport efficiency between fluids and particles. On the other hand, when α< 0, i.e., the pressure gradient increases in the flow direction, it can cause backflow, as shown

in **Figure 5a**. Since local and average shear stress are both defined as the shear stress at the plate, the behavior of the velocity at the first phase and the behavior of the local and average shear stress are shown as identical; these are illustrated in **Figure 5b**,**c**.

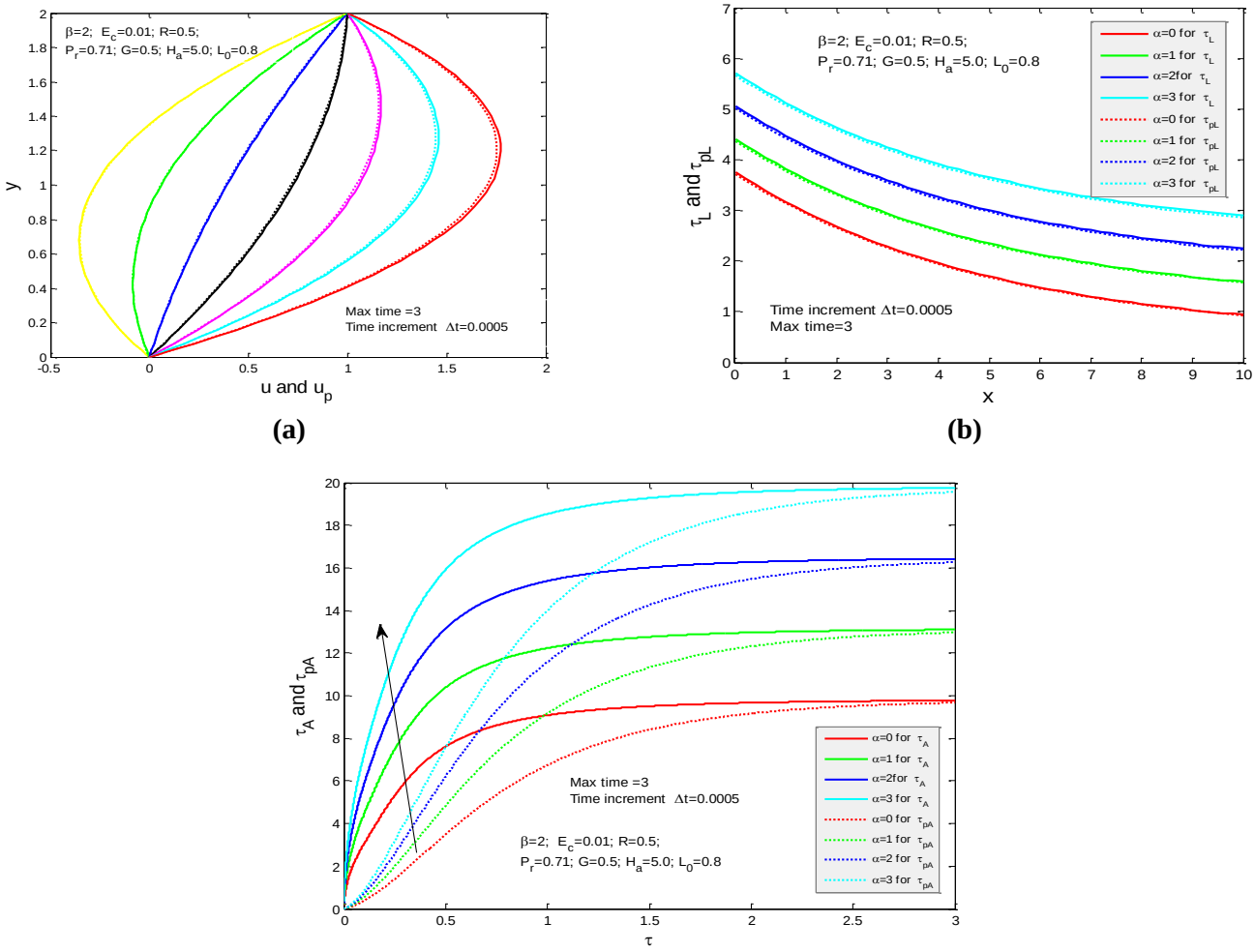

Figure 5. Effects of pressure gradient parameter α on **(a)** velocity; **(b)** local shear stress τ_L (or τ_{pL}); and **(c)**average shear stress τ_A (or τ_{pA}).

Figure 6a–c show an increase in velocity, local shear stress, and average shear stress with the Casson parameter, indicating that a higher yield stress results in greater resistance to fluid flow. This resistance allows the fluid to achieve higher flow rates while also experiencing greater internal friction. For dust particles suspended in fluid, increased shear stress improves their velocity and promotes greater dispersion, increasing mixing and overall stability.

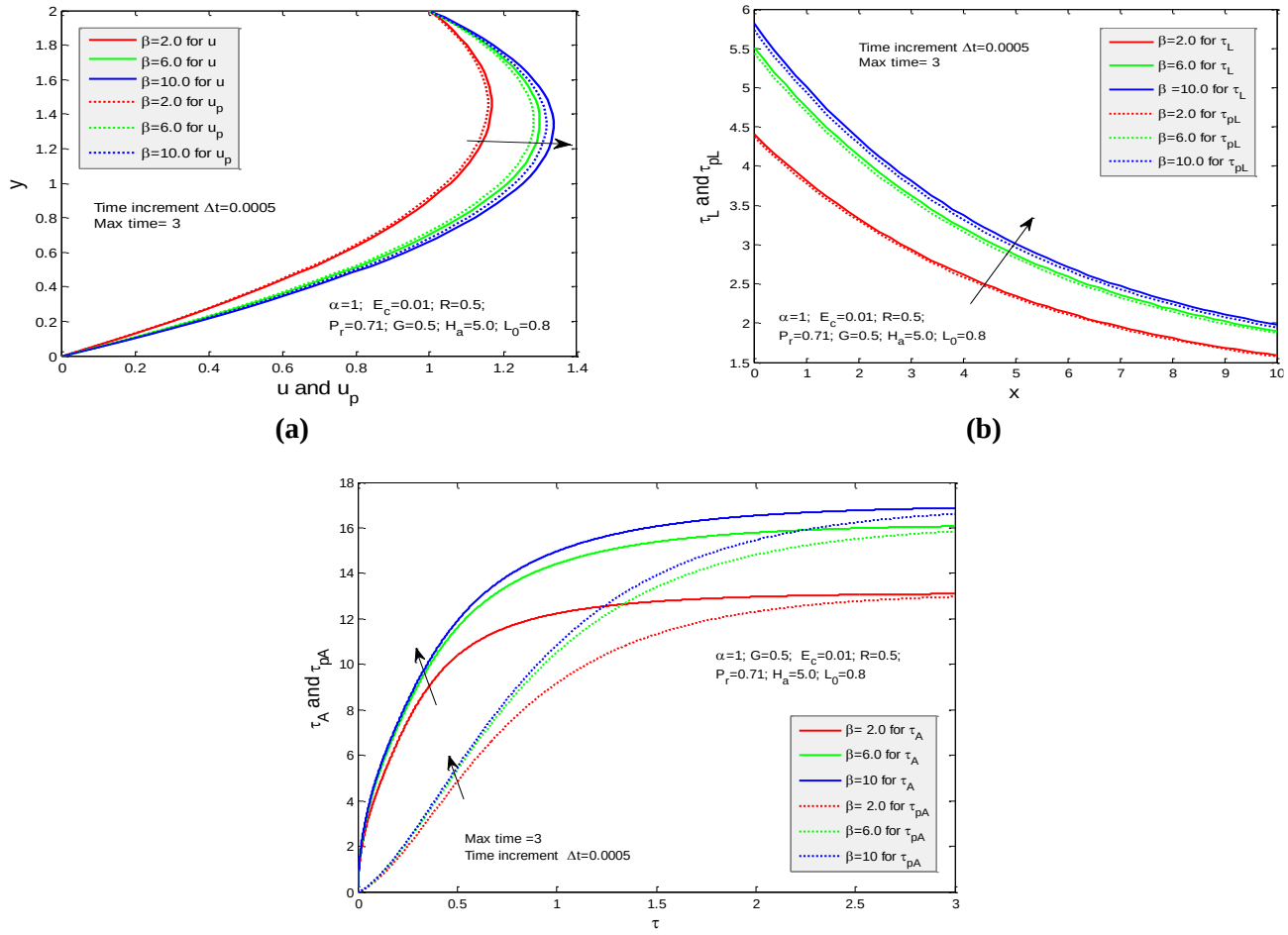

Figure 6. Effects of Casson parameter β on **(a)** velocity; **(b)** local shear stress τ_L (or τ_{pL}); and **(c)** average shear stress τ_A (or τ_{pA}).

Figure 7a–c illustrate the effect of different Hartmann numbers on velocity, local shear stress, and average shear stress. It is observed that the local and average shear stress increases as the modified Hartmann number increases. Similarly, for dust particles, shear stress also increases with a higher modified Hartmann number. This indicates that strong magnetic fields increase the resistance to fluid flow, resulting in high shear stress in both the fluid phase and the dust phase.

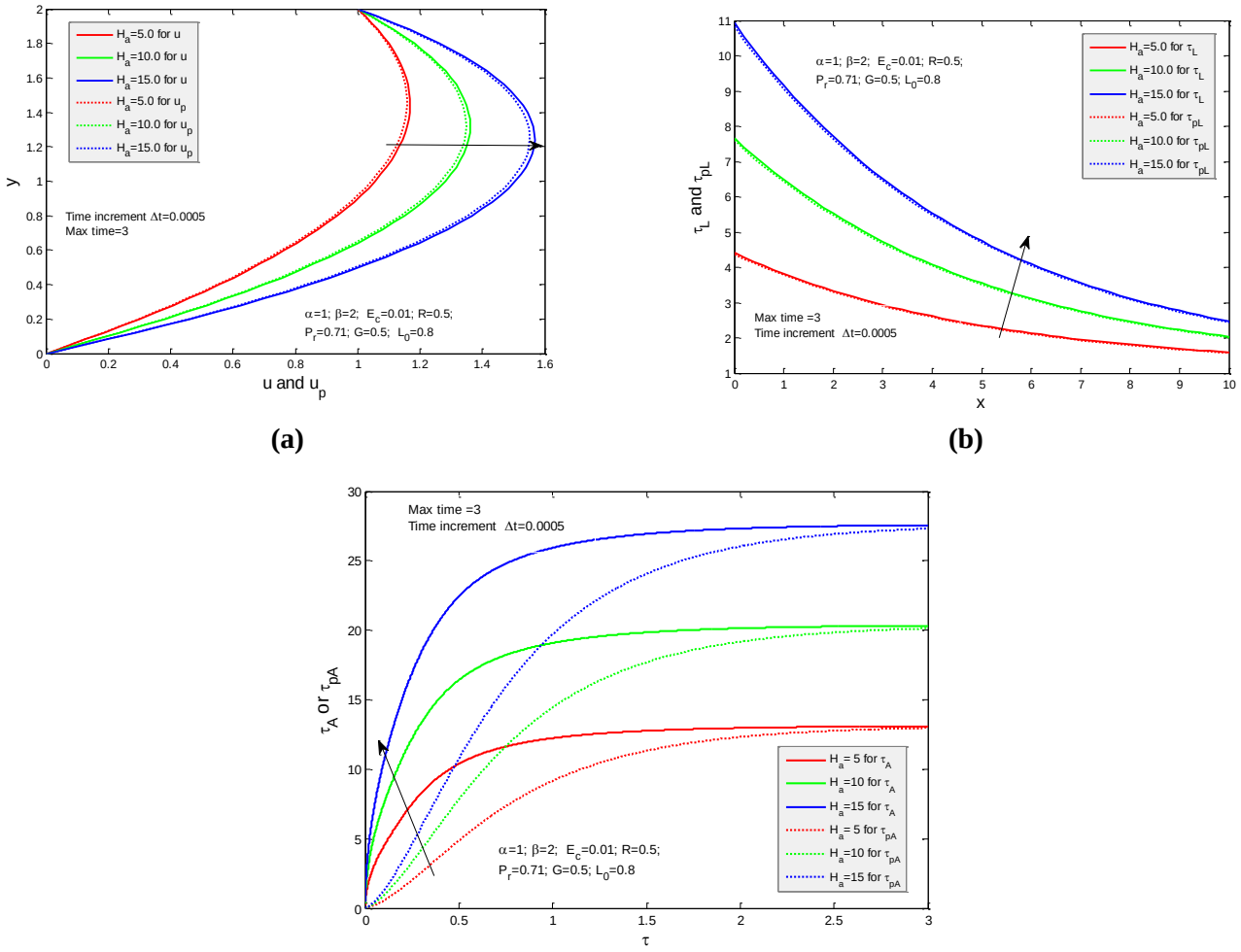

Figure 7. Effects of modified Hartmann number H_a on **(a)**velocity; **(b)** local shear stress τ_L (or τ_{pL}); and **(c)**average shear stress τ_A (or τ_{pA}).

Figure 8a–c illustrate the effect of particle mass parameters on velocity, local shear stress, and average shear stress. As the particle mass parameter increases, the local and average shear stress decreases. This trend is also observed for dust particles, suggesting that a higher particle mass parameter reduces the shear stress in both the fluid phase and the dust phase.

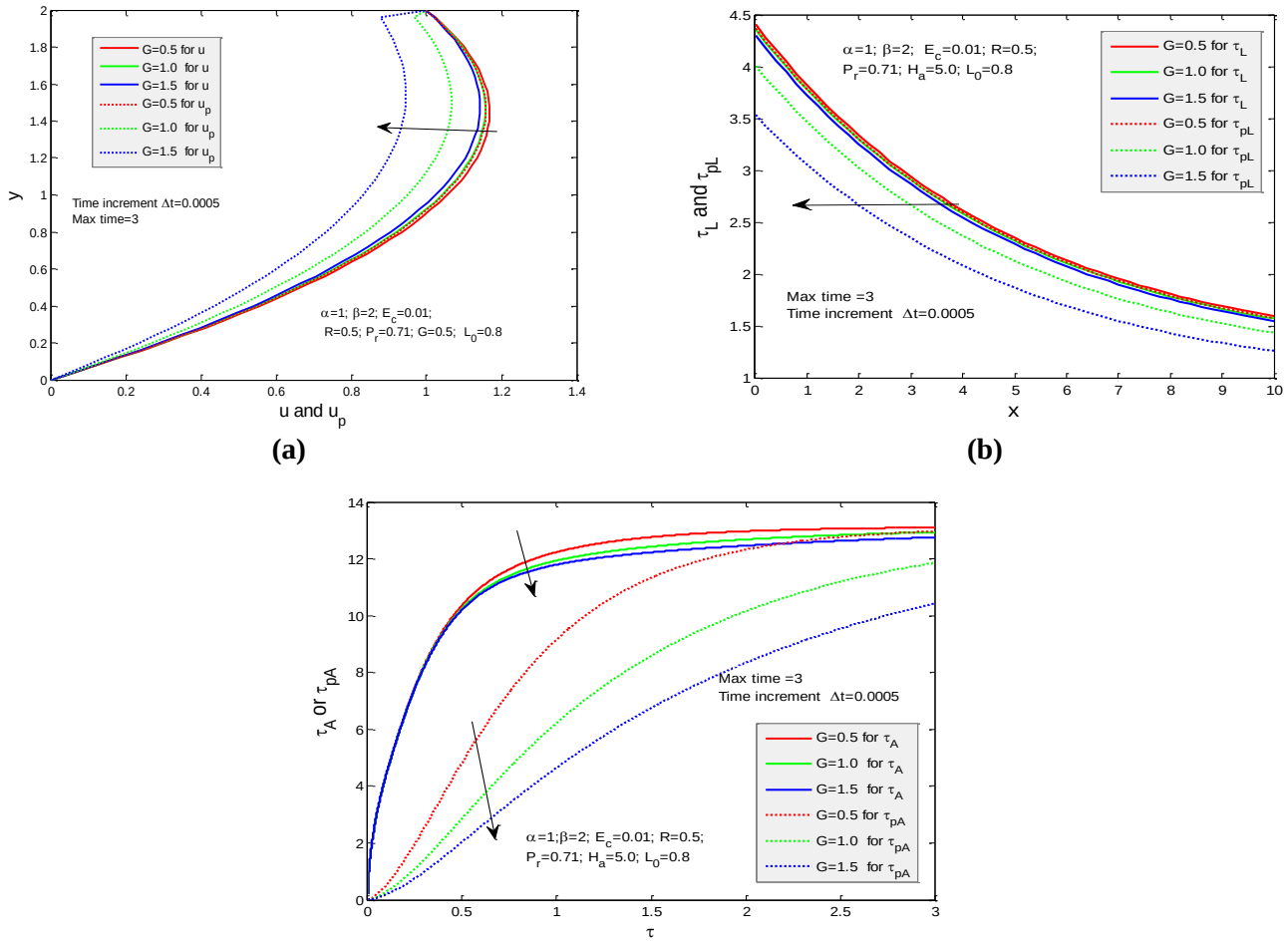

Figure 8. Effects of particle mass parameter *G* on **(a)** velocity; **(b)** local shear stress τ_L (or τ_{pL}); and **(c)**average shear stress τ_A (or τ_{pA}).

Figure 9a–c illustrate the effects of the fluid concentration parameter on velocity, local shear stress, and average shear stress. The results show that an increase in the fluid concentration parameter results in a decrease in both local and average shear stresses. Similar trends are noted for the dust particles, indicating that a higher fluid concentration is associated with reduced shear stresses in both phases.

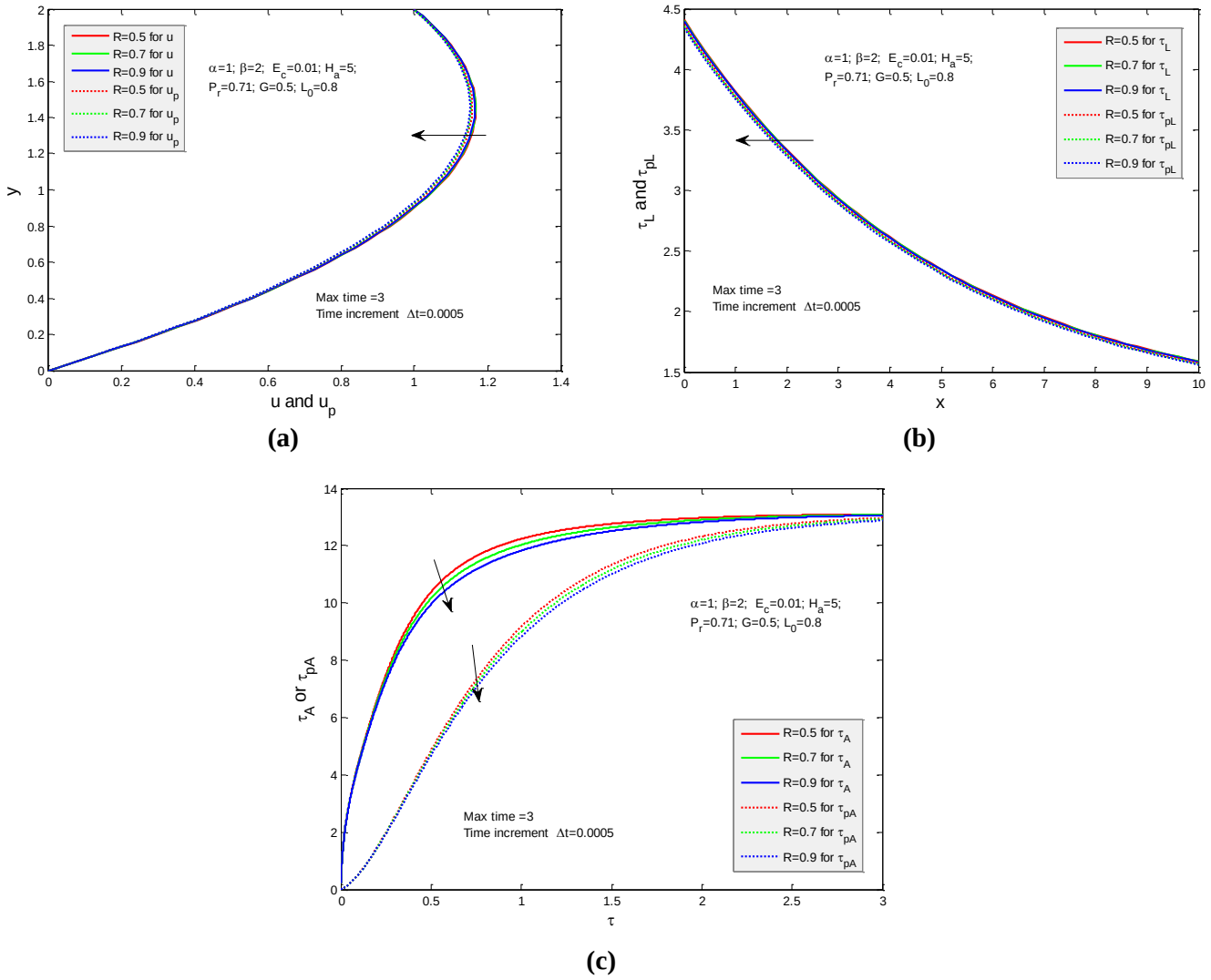

Figure 9. Effects of fluid concentration parameter R on **(a)** velocity; **(b)** local shear stress τ_L (or τ_{pL}); and **(c)**average shear stress τ_A (or τ_{pA}).

4.3.2. Impacts of relevant parameters on temperature, local Nusselt number and average Nusselt number

Figures 10–17 demonstrate the distribution of temperature, the local and average Nusselt number for various values of α, β, H_a, P_r, R, G , L_0 and E_c.

Figure 10a shows the effect of the pressure gradient parameter on θ (or θ_p) and the local Nusselt number, and the average Nusselt number Nu_A (or Nu_{AL}). It is observed that as the pressure gradient parameter increases, the temperature for both the fluid phase and the dust particles also rises. This trend can be attributed to enhanced energy transfer resulting from the increased pressure gradient, which promotes better mixing and heat distribution within the fluid. **Figure 10b**,**c** present the local and average Nusselt numbers, respectively, indicating that both the local and average Nusselt numbers decrease with increasing temperature for both clear fluids and dust particles. This inverse relationship suggests that higher temperatures may reduce heat

transfer efficiency, possibly due to changes in viscosity and thermal properties that affect fluid dynamics and interactions between the fluid and dust particles.

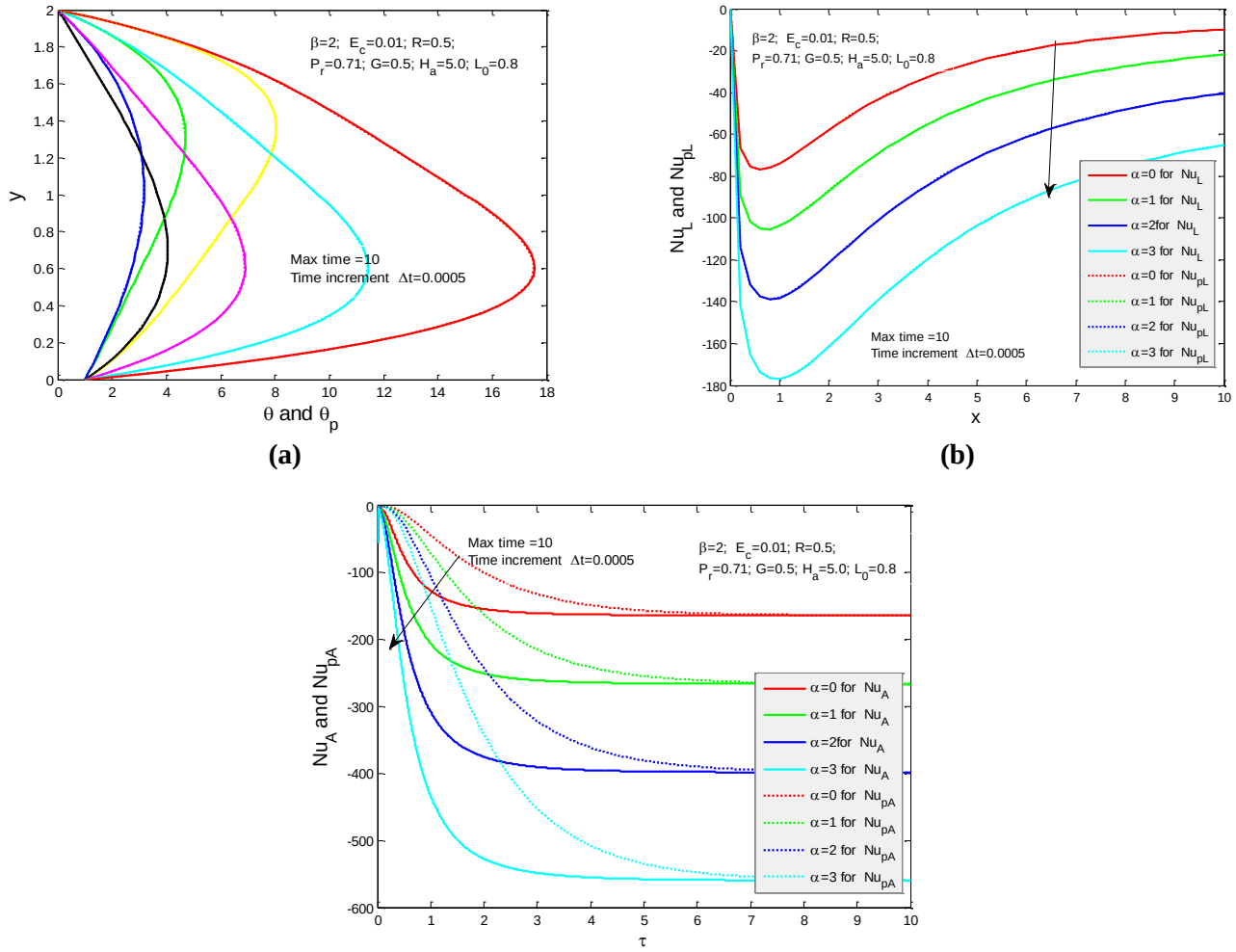

Figure 10. Effects of pressure gradient parameter α on **(a)** temperature; **(b)** local Nusselt number Nu_L (or Nu_{pL}); **(c)** average Nusselt numberNu_A (or Nu_{AL}).

Figure 11a–c illustrate how temperature distributions θ (or θ_p), as well as local and average Nusselt numbers Nu_L (or Nu_{pL}), vary with the Casson parameter (β). The increase in temperature profiles indicates that the fluid may become more efficient at transferring heat to surfaces. As the Casson parameter rises, it suggests that the fluid experiences greater resistance to flow, which can improve thermal energy retention. Consequently, the fluid can sustain higher temperatures due to reduced convective heat loss. However, the local and average Nusselt numbers exhibit the opposite effect, decreasing as the Casson parameter increases.

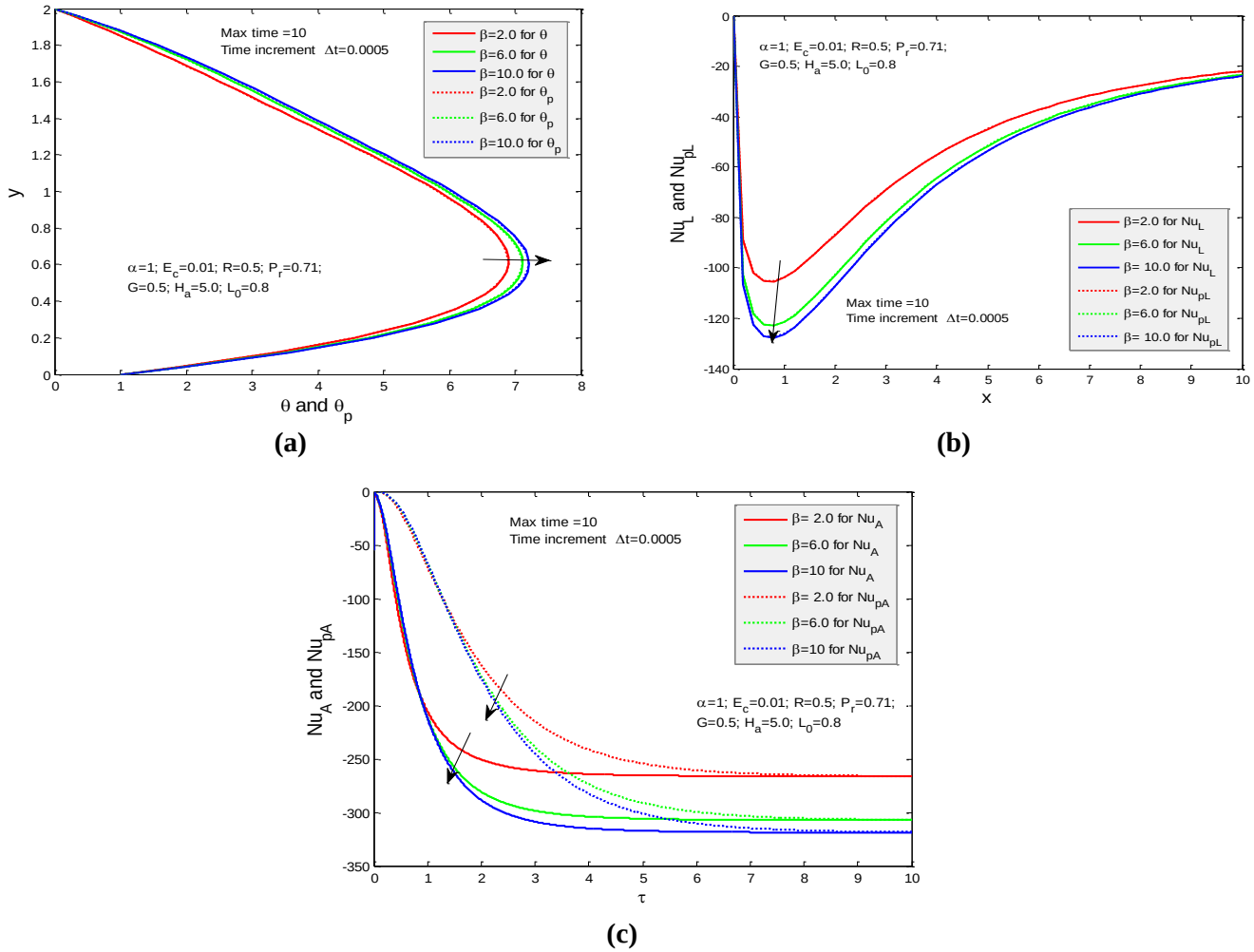

Figure 11. Effects of Casson parameter β on **(a)** temperature; **(b)** local Nusselt number Nu_L (or Nu_{pL}); **(c)** average Nusselt number Nu_A (or Nu_{AL}).

Figure 12a illustrates the effect of the modified Hartmann number on the temperature distribution. As the modified Hartmann number increases, the temperatures within the fluid rise, likely due to the magnetic field's influence, which enhances heat retention. Conversely, the local and average Nusselt numbers shown in **Figure 12b**,**c** exhibit a downward trend with an increase in the modified Hartmann number. This indicates that while temperatures are increasing, the efficiency of heat transfer is decreasing. The stronger magnetic forces may lead to a more stable fluid flow, reducing turbulence and, consequently, the effectiveness of convective heat transfer, which negatively impacts the overall heat transfer performance in the system.

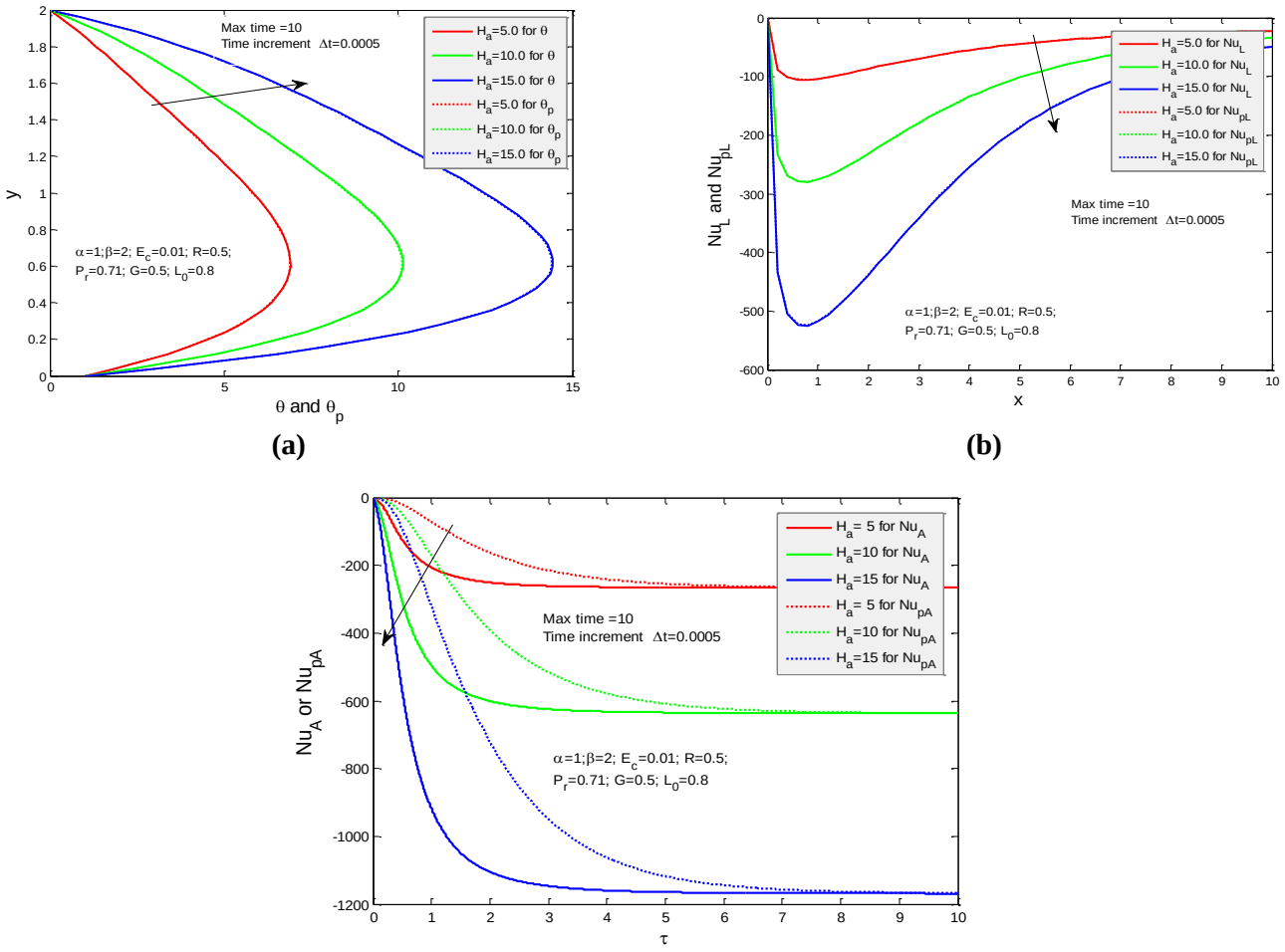

Figure 12. Effects of modified Hartmann number H_a on **(a)** temperature; **(b)** local Nusselt number Nu_L (or Nu_{pL}); **(c)** average Nusselt number Nu_A (or Nu_{AL}).

Figure 13a illustrates the impact of the particle mass parameter on temperature distribution. As the fluid concentration parameter increases, the temperature also rises, though the change is relatively small. The more significant effects are emphasized in the zoomed-in section of **Figure 12b**, which clearly highlights these subtle variations. Additionally, the local and average Nusselt numbers presented in **Figure 13b**,**c** show an increasing trend with higher fluid concentration. This increase suggests that as the fluid concentration rises, the efficiency of heat transfer improves. The enhanced Nusselt numbers indicate that variations in concentration may modify the flow characteristics, resulting in better convective heat transfer within the system.

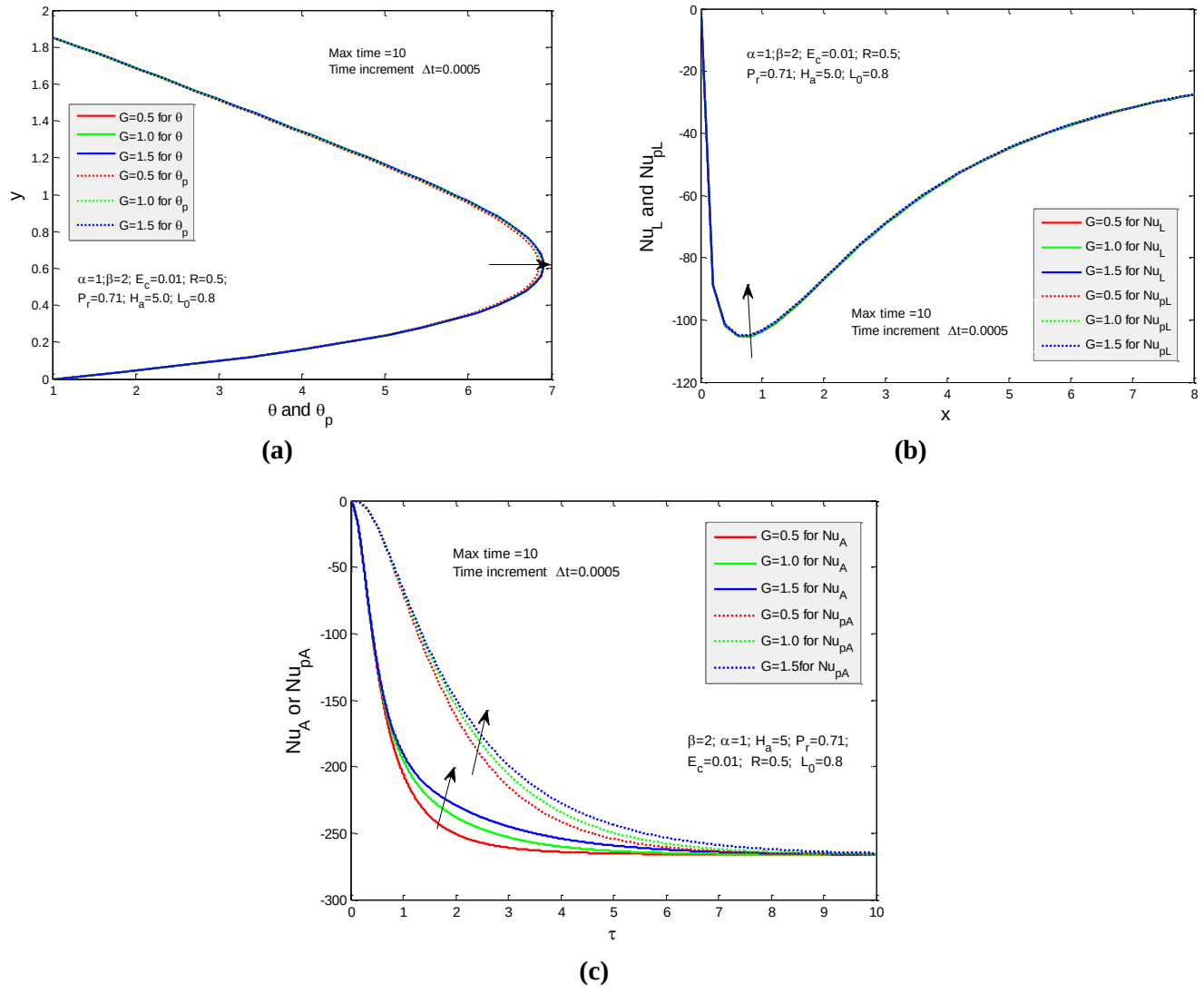

Figure 13. Effects of Eckert number E_c on **(a)** temperature; **(b)** local Nusselt number Nu_L (or Nu_{pL}); **(c)** average Nusselt number Nu_A (or Nu_{AL}).

Figure 14a shows that the temperature increases with higher values of the Eckert number for both the fluid phase and the dust particles. The local and average Nusselt numbers are illustrated in **Figure 14b**,**c**, respectively. Analysis of these figures reveals an inverse relationship between both the local and average Nusselt numbers and temperature for both the clear fluid and the dust particles. This indicates that although higher temperatures result from increased Eckert numbers, the efficiency of heat transfer diminishes. This phenomenon indicates that increased temperature can affect flow characteristics, ultimately reducing the efficiency of convective heat transfer within the system.

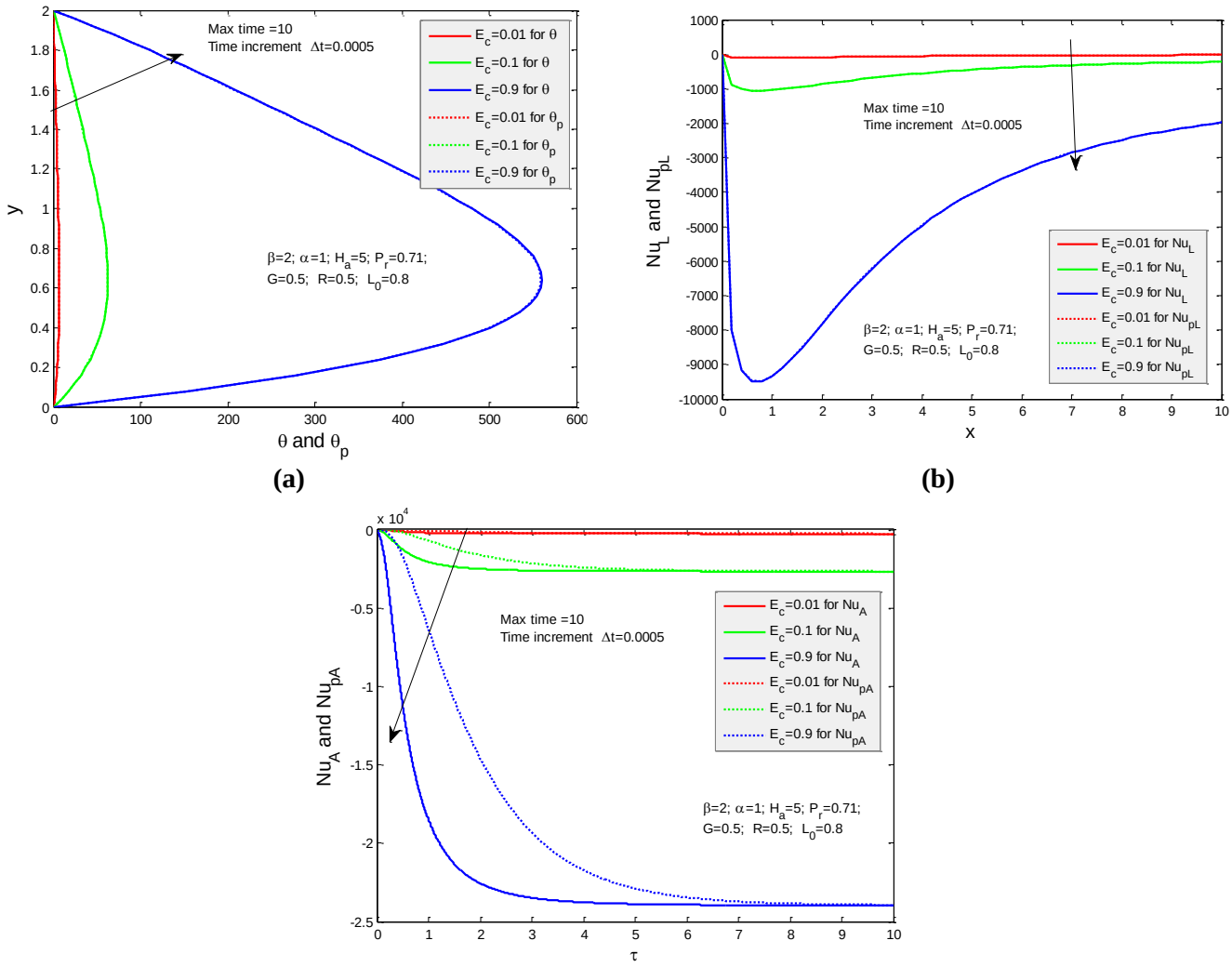

Figure 14. Effects of Eckertnumber E_c on **(a)** temperature; **(b)** local Nusselt number Nu_L (or Nu_{pL}); **(c)** average Nusselt number Nu_A (or Nu_{AL}).

Figure 15a shows a slight decrease in temperature as the fluid density parameter increases for both the fluid phase and dust particles. The local and average Nusselt numbers are plotted in **Figure 15b**,**c** respectively. An examination of these figures reveals an inverse relationship between both the local and average Nusselt number and temperature for clear fluids and dust particles. This suggests that the temperature decreases slightly as the fluid density increases, which negatively affects the heat transfer efficiency. The observed decrease in the Nusselt number indicates that fluid density variations can significantly affect the convective heat transfer characteristics within the system.

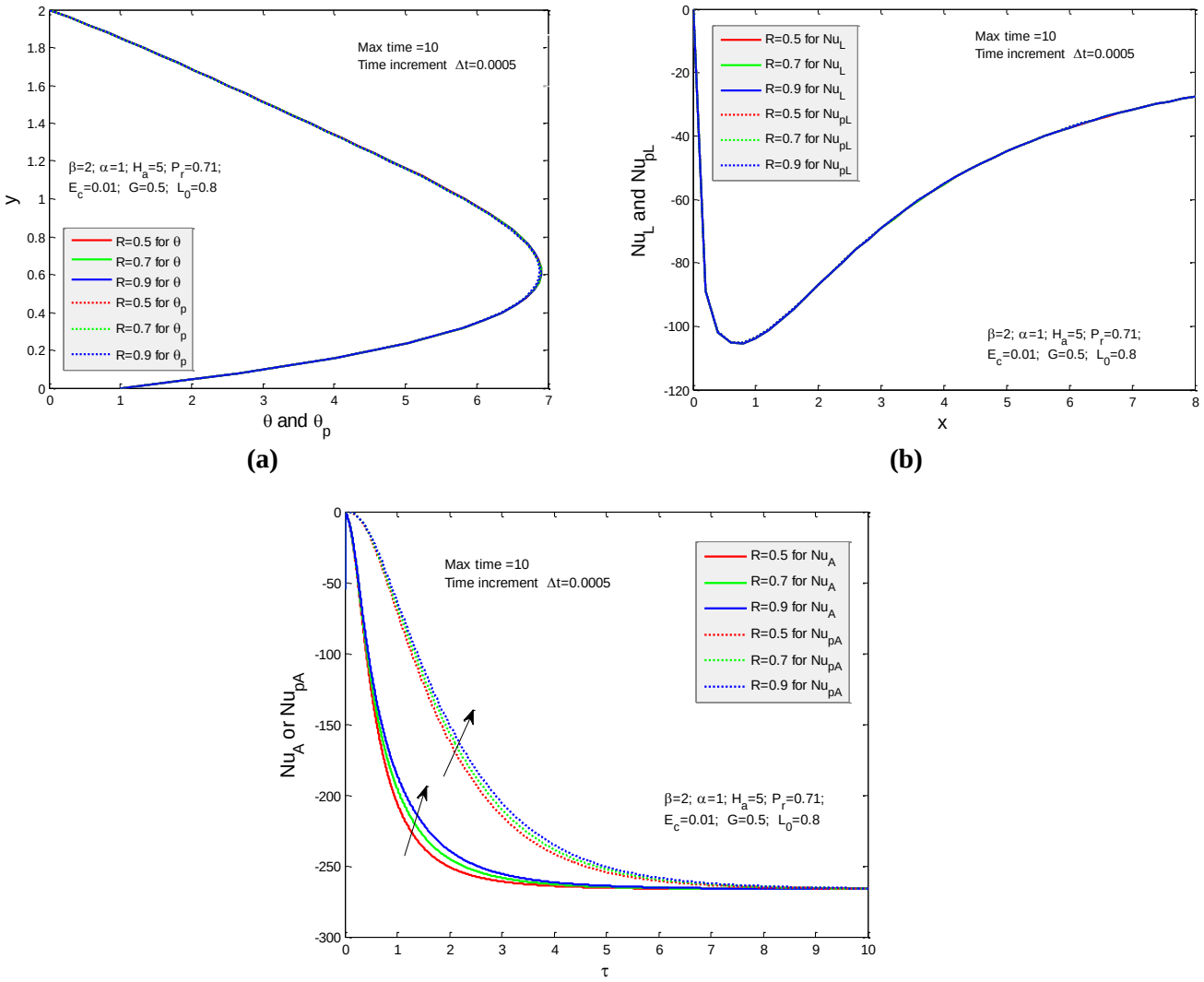

Figure 15. Effects of fluid concentration parameter *R*on **(a)** temperature; **(b)** local Nusselt number Nu_L (or Nu_{pL}); **(c)** average Nusselt number Nu_A (or Nu_{AL}).

Figure 16a illustrates the slight increase in temperature with increasing relaxation time parameters for both the fluid phase and dust particles. **Figure 16b**,**c** present the local and average Nusselt numbers, respectively. An analysis of these figures reveals an inverse relationship between both the local and average Nusselt numbers and temperature for clear fluids and dust particles. This suggests that as the temperature increases slightly with a larger relaxation time, the heat transfer efficiency decreases. This behavior can be linked to the effect of relaxation time on fluid viscosity and flow dynamics, which can inhibit effective convective heat transfer within the system.

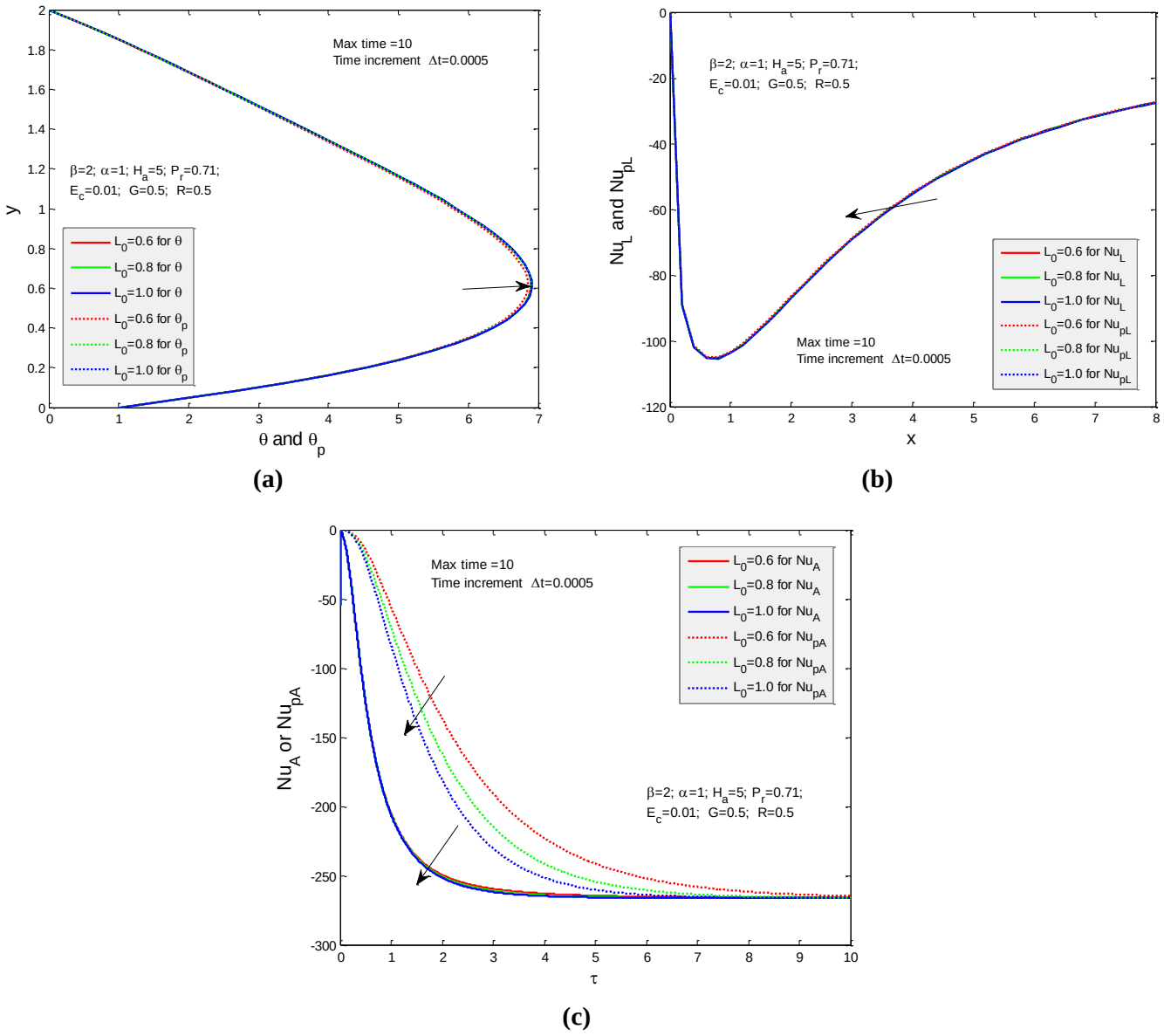

Figure 16. Effects of relaxation time parameter L_0 on **(a)** temperature; **(b)** local Nusselt number Nu_L (or Nu_{pL}); **(c)** average Nusselt number Nu_A (or Nu_{AL}).

Figure 17a illustrates the impact of the Prandtl number on the temperature profile. As the Prandtl number increases, the temperature shows an upward trend. However, **Figure 17b**,**c** indicate that both the local and average Nusselt numbers decrease as the Prandtl number rises for both the clear fluid and the dust particles. This suggests that, while higher Prandtl numbers are associated with elevated temperatures, they also correlate with a reduction in heat transfer efficiency. This phenomenon may imply that changes in the fluid's thermal properties, influenced by the Prandtl number, hinder effective convective heat transfer within the system.

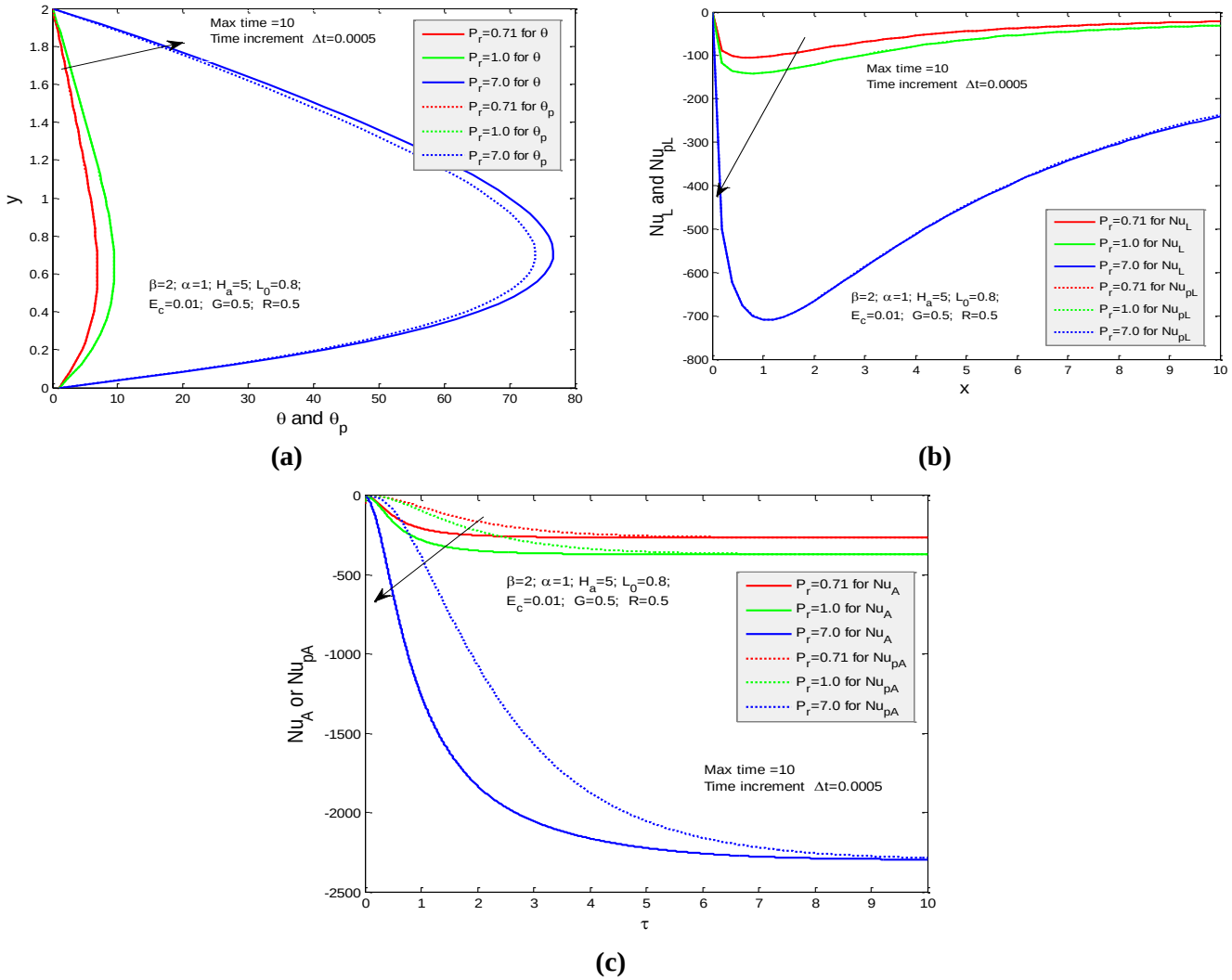

Figure 17. Effects of the Prandtl parameter P_r on **(a)** temperature; **(b)** local Nusselt number Nu_L (or Nu_{pL}); **(c)** average Nusselt number Nu_A (or Nu_{AL}).

5. Conclusions

The initiation of fluid motion is achieved by applying a uniform magnetic force generated by the Riga plate combined with a pressure gradient force acting on the fluid. The mathematical model governing this system is based on a specific set of partial differential equations that describe the behavior of the dusty Casson fluid. Dusty fluids often exhibit intricate interactions between the fluid and the suspended particles, with fluid particles moving faster than the dust particles and tending to travel parallel to one another. To reach a steady-state solution, the velocity of the fluid must exceed that of the dust particles. Although the velocities of the dust particles do not align with those of the fluid particles at a steady state, their temperatures equilibrate after a certain time step. Furthermore, several other significant findings are summarized below:

- The velocities of both fluid particles and dust particles increase with an increasing pressure gradient parameter and modified Hartmann number. In contrast, these

velocities decrease as the Casson parameter, concentration parameter, and particle mass parameter increase.

- The temperature distributions for both fluid and dust particles increase with higher values of the Eckert number, relaxation time parameter, and Prandtl number. In contrast, the particle mass parameter decreases these temperature distributions.
- The same effects observed for the velocities are also seen in the local and average shear stress of both fluid and dust particles.
- However, for temperature, the thermal boundary layer thickness and heat transfer rate at the plate exhibit opposite effects compared to the temperature distribution of both fluid and dust particles.

This investigation could broaden the scope of our study and open up avenues for applications in fields such as material processing, biomedical engineering, and energy systems. In the future, we are interested in investigating the aforementioned topic.

Author contributions: Conceptualization, MRI and SN; methodology, SN; software, MRI; validation, MMA, RNM and MRI; formal analysis, SN; investigation, MRI; resources, RNM; data curation, MMA; writing—original draft preparation, SN; writing—review and editing, MRI; visualization, MMA; supervision, MMA. All authors have read and agreed to the published version of the manuscript.

Institutional review board statement: Not applicable.

Informed consent statement: Not applicable.

Data availability statement: The data supporting the findings of this study are available from the corresponding author upon reasonable request.

Conflict of interest: The authors declare no conflict of interest.

References

1. Casson N. A Flow Equation for Pigment Oil Suspensions of the Printing Ink Type. In: Mill CC (editors). Rheology of Disperse Systems. Pergamon Press; 1959. pp. 84–102.
2. Gailitis A, Leilausis O. On a possibility to reduce the hydro dynamical resistance of a plate in an electrode. Appl. Magneto hydrodyn. 1961; 12: 143–146.
3. Saffman PG. On the stability of laminar flow of a dusty gas. J. Fluid Mech. 1962; 13(1): 120–128.
4. Eldabe NTM, Salwa MGE. Heat transfer of MHD Non-Newtonian Casson Fluid Flow between two Rotating Cylinders. Journal of the Physical Society of Japan. 1995; 64: 41–64.
5. Fang T. A note on the incompressible Couette flow with porous walls. International Communication in Heat and Mass Transfer. 2004; 31(1):31–41.
6. Boyd J, Buick JM, Green S. Analysis of the Casson and Carreau-Yasuda non-Newtonian blood models in steady and oscillatory flows using the lattice Boltzmann method.Physics of Fluid. 2007; 19: 093103.
7. Damseh RA. On Boundary Layer Flow of a Dusty Gas from a Horizontal Circular Cylinder. Brazilian Journal of Chemical Engineering.2010; 27(4): 653–662.
8. Makinde OD, Chinyoka T. MHD transient flows and heat transfer of dusty fluid in a channel with variable physical properties and Navier slip condition. Computers and Mathematics with Applications. 2010; 60(3): 660–669.
9. Eguia P, Zueco J, Granada E, Patino D. NSM solution for unsteady MHD Couette flow of a dusty conducting fluid with variable viscosity and electric conductivity. Applied Mathematical Modelling. 2011; 35(1): 303–316.
10. Hayat T, Shehzad SA, Alsaedi A. Soret and Dufour Effects on Magnetohydrodynamic (MHD) Flow of Casson Fluid. Applied Mathematics and Mechanics. 2012; 33: 1301–1312.

11. Nadeem S, Haq RU, Akber NS, Khan ZH. MHD three-dimensional Casson fluid flow past a porous linearly stretching sheet. Alexandria Engineering Journal. 2013; 52(4): 577–582.
12. Ramesh GK, Gireesha BJ. Flow Over a Stretching Sheet in a Dusty Fluid With Radiation Effect. Journal of Heat Transfer. 2013; 135(10): 102702.doi: 10.1115/1.4024587
13. Mukhopadhyay S, Ranjan De P, Bhattacharyya K, Layek GC. Casson fluid flow over an unsteady stretching surface. Ain Shams Engineering Journal. 2013; 4(4): 933–938.
14. Attia HA, Aboul-Hassan AL, Abdeen MAM, El-Din Abdin A. MHD flow of a dusty fluid between two infinite parallel plates with temperature dependent physical properties under exponentially decaying pressure gradient. Bulgarian Chemical Communications. 2014; 46(2): 320–329.
15. Pramanik S. Casson fluid flow and heat transfer past an exponentially porous stretching surface in presence of thermal radiation.Ain Shams Engineering Journal. 2014; 5(1): 205–212.
16. Ramesh K, Devakar M. Some analytical solutions for flows of Casson fluid with slip boundary conditions. Ain Shams Engineering Journal. 2015; 6(3): 967–975.
17. Abbas T, Ayub M, Bhatti MM, et al. Entropy generation on nanofluid flow through a horizontal Riga plate. Entropy. 2016; 18(6).
18. Raju CSK, Sandeep N, Sugunamma V, et al. Heat and Mass Transfer in Magnetohydrodynamic Casson Fluid over an Exponentially Permeable Stretching Surface. Engineering Science and Technology. 2016; 19(1): 45–52.
19. Awais M, Malik MY, Hussain A, et al. A Computational Analysis Subject to Thermophysical Aspects of Sisko Fluid Flow over a Cylindrical Surface. The European Physical Journal Plus. 2017; 132: 1–16. doi: 10.1140/epjp/i2017-11645-y
20. Isa SM, Mohammad NF. Boundary Layer Flow of Dusty Fluid on a Stretching Sheet of Another Quiescent Fluid.Journal of Physics: Conference Series. 2017; 819(1).
21. Jalil M, Asghar S, Yasmeen S. An Exact Solution of MHD Boundary Layer Flow of Dusty Fluidover a Stretching Surface. Mathematical Problems in Engineering. 2017. doi: 10.1155/2017/2307469
22. Anjum A, Mir NA, Farooq M, et al. Influence of thermal stratification and slip conditions on stagnation point flow towards variable thicked Riga plate. Results in Physics. 2018; 9: 1021–1030.
23. Mohamed Ismail A, Rahuman S, Sampath Kumar K. A Solution of Unsteady Magnetohydrodynamic flow of dusty fluid between parallel porous plates. International Journal of Pure and Applied Mathematics. 2018; 119(15): 1221–1232.
24. Ahmad A. Flow Control of Non-Newtonain Fluid using Riga Plate: Reiner-Phillipoff and Powell-Eyring Viscosity Models. Journal of Applied Fluid Mechanics. 2019; 12(1): 127–133.
25. Attia HA, Ewis KM. Magnetohydrodynamic flow of continuous dusty particles and non-Newtonian Darcy fluids between parallel plates. Advances in Mechanical Engineering. 2019; 11(6): 1–11.
26. Khan D, Kumam P, Kumam W, et al. Relative magnetic field and slipping effect on Casson dusty fluid of two phase fluctuating flow over inclined parallel plate. South African Journal of Chemical Engineering. 2023; 44: 135–146.
27. Jalili B, Azar AA, Jalili P, Ganji DD. Impact of variable viscosity on asymmetric fluid flow through the expanding/contracting porous channel: A thermal analysis. Case Studies in Thermal Engineering. 2023; 52:103672
28. Khan MWS, Asghar Z, Hafeez A. Graetz problem for the casson fluid model with prescribed heat flux in a circular duct. The European Physical Journal Special Topics. 2023; 233; 1349–1358. doi: 10.1140/epjs/s11734-023-00957-8
29. Khan MWS, Ali N. Theoretical analysis of thermal entrance problem for blood flow: An extension of classical Graetz problem for Casson fluid model using generalized orthogonality relations. International Communications in Heat and Mass Transfer. 2019; 109. doi: 10.1016/j.icheatmasstransfer.2019.104314
30. Khan MWS, Asghar Z, Shatanawi W, Gondal MA. Thermal entry problem for a tube with prescribed heat flux condition using viscoplastic fluid: An extended Graetz problem for Casson fluid with axial conduction and viscous dissipation. ZAMM-Journal of Applied Mathematics and Mechanics. 2024; 104(4): 1–14.doi: 10.1002/zamm.202300109
31. Paul A, Das TK, Nath JM. Numerical investigation on the thermal transportation of MHD Cu/Al_2O_3-H_2O Casson-hybrid-nanofluid flow across an exponentially stretching cylinder incorporating heat source. Physica Scripta. 2022; 97(8). doi: 10.1088/1402-4896/ac7981